Geomechanics and Engineering, *Vol. 33, No. 5 (2023) 477-486*
https://doi.org/10.12989/gae.2023.33.5.477

Investigation of the behavior of a tunnel subjected to strike-slip fault rupture with experimental approach

Zhen Cui[1], Tianqiang Wang*[2], Qian Sheng[1] and Guangxin Zhou[1]

[1]*State Key Laboratory of Geomechanics and Geotechnical Engineering, Institute of Rock and Soil Mechanics, Chinese Academy of Sciences, Wuhan, Hubei 430071, China*
[2]*Key Laboratory of Transportation Tunnel Engineering, Ministry of Education, School of Civil Engineering, Southwest Jiaotong University, Chengdu, 610031, China*

(*Received July 15, 2022, Revised March 8, 2023, Accepted March 28, 2023*)

Abstract. In the studies on fault dislocation of tunnel, existing literatures are mainly focused on the problems caused by normal and reverse faults, but few on strike-slip faults. The paper aims to research the deformation and failure mechanism of a tunnel under strike-slip faulting based on a model test and test-calibrated numerical simulation. A potential faulting hazard condition is considered for a real water tunnel in central Yunnan, China. Based on the faulting hazard to tunnel, laboratory model tests were conducted with a test apparatus that specially designed for strike-slip faults. Then, to verify the results obtained from the model test, a finite element model was built. By comparison, the numerical results agree with tested ones well. The results indicated that most of the shear deformation and damage would appear within fault fracture zone. The tunnel exhibited a horizontal S-shaped deformation profile under strike-slip faulting. The side walls of the tunnel mainly experience tension and compression strain state, while the roof and floor of the tunnel would be in a shear state. Circular cracks on tunnel near fault fracture zone were more significant owing to shear effects of strike-slip faulting, while the longitudinal cracks occurred at the hanging wall.

Keywords: deformation profile; failure pattern; strain distribution features; strike-slip fault; water conveyance tunnel

1. Introduction

In east Asia, the western region of China is known for the existence of large numbers of seismic zones and active faults. However, with the increase on economic development in this region, massive infrastructure constructions such as high-speed railway tunnels and long-distance water conveyance tunnels, are carried or carrying out. For these tunnels that across active faults, the tunnels would inevitably be affected by the tectonic movement of faults (Cui *et al.* 2022).

Active faults can be roughly divided into stick-slip faults and creep faults, based on the dislocation velocity. Normal fault, reverse fault, and strike-slip fault can be distinguished according to the kinematics mechanism (Yan *et al.* 2021).

Due to the difficultly in in-situ monitoring, pioneer researchers attempted to investigate this issue with experimental and numerical approaches. Representative works can be referenced as Lin *et al.* (2007), Baziar *et al.* (2014), Jalali *et al.* (2016), and Melissianos *et al.* (2017). As a typical example, Jalali *et al.* (2016) revealed the failure mechanism of a buried steel gas pipelines affected by reverse faulting based on model experiments and numerical simulations. In their experiments, it is confirmed that an S-shape deformation along pipelines was exhibited. Two buckling sections occurs where the stress exceeds the yielding limit. Similar research approaches were performed by Lin *et al*. (2007) for tunnels, crack propagation in the soil, damage distribution and deformation in the tunnel were investigated. In longitudinal tunnel, active length of a tunnel also has been ascertained based on a series of centrifuge tests (Yao *et al.* 2021).

Moreover, efforts on normal faults have been made (Kiani *et al.* 2016, Liu *et al.* 2015, Huang *et al.* 2017, Cai *et al.* 2019, Sabagh and Ghalandarzadeh 2020). For instance, a scaled physical modelling was conducted to reappear the normal faulting process with various dip angles of fault in Kiani *et al*. (2016). The deformation of a segmental tunnel under normal faulting was obtained by a series of centrifuge tests. Wang (2022, 2023) investigated the deformation and failure of mining method tunnel when the tunnel was affected by normal faulting. Qiao *et al.* (2022) constructed a 3D normal faulting numerical model to study longitudinal tunnel mechanical response and found that oval effect of tunnel sections was main deformation pattern owing to compression.

In strike-slip faults, existing researches are mainly produced by numerical simulation methods (Shahidi and Vafaeian 2005, Melissianos *et al.* 2016, Zhong *et al.* 2020, Zaheri *et al.* 2020, Zeng *et al.* 2021). As a typical example, in Shahidi and Vafaeian (2005), a beam model was adopted in a 3D longitudinal model subjected to a faulting. The structural design parameters in flexible joints were estimated respectively. In Vazouras *et al.* (2010, 2012), a simulation on a buried fault-crossing steel pipelines was performed. Zhong *et al.* (2020) proposed two quantitative

*Corresponding author, Ph.D.
E-mail: tqwang@my.swjtu.edu.cn

ISSN: 2005-307X (Print), 2092-6219 (Online)

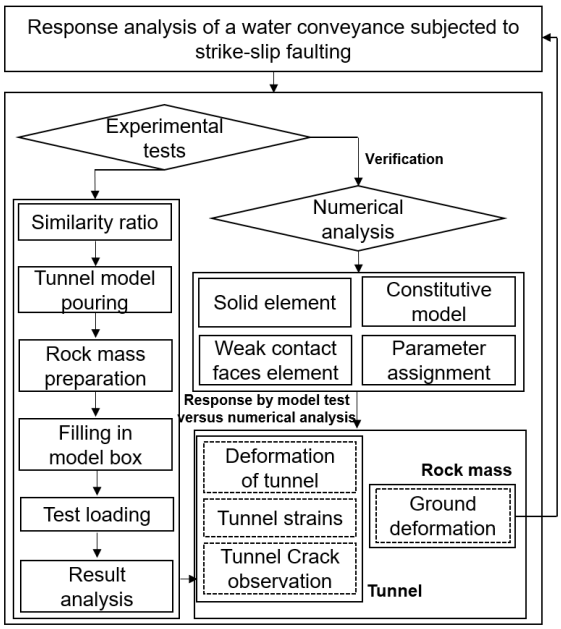

Fig. 1 Flow chart for the research of tunnel response under strike-slip faulting

damage indices to evaluate the structural damage for a strike-slip fault-crossing mountain tunnel. The literature also indicated that the structural damages were mainly focused on the fault fracture zone, while the fault dip was a critical parameter when a tunnel was disturbed by a fault dislocation.

Overall, the limited knowledges in strike-slip fault dislocation mechanism and tunnel damage attribute to insufficient concerns. Research concerning the physical scaled model test for tunnels across a strike-slip fault has been seldom reported. In this study, based on a real prototype water conveyance tunnel in China, a scaled model test was performed for a tunnel model under the loading of strike-slip fault dislocation. The deformation of rock mass and tunnel, and crack propagation of tunnel were measured. Based on the test data, a 3D numerical model was built. In conjunction with the experimental and numerical results, the response mechanism and failure feature of the tunnel were revealed furtherly when the strike-slip fault dislocation appeared in the stratum. A flow chart has been drawn below to illustrate the logic of this study, as shown in Fig. 1.

2. Experimental tests

2.1 Apparatus and model

A self-designed scale model experiment apparatus shown in Fig. 2 was adopted in the test. The dimension of the model box is 72 cm in length, 50 cm in width, and 40 cm in height, respectively. The shear box is composed of a fixed half and a moving half, which represent the hanging wall and foot wall. The moving plate of the shear box is connected with a hydraulic jack over a steel plate. And driven by the hydraulic jack, the moving half can move

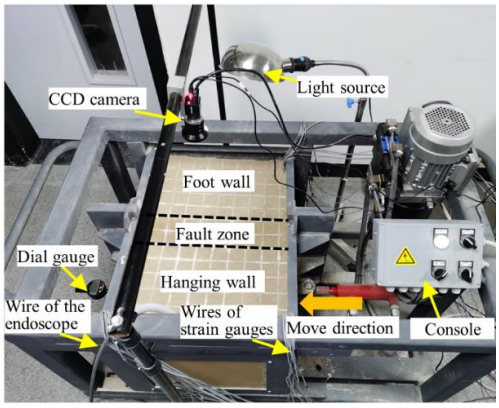

Fig. 2 Setup of the model test apparatus

horizontally, as to represents the strike-slip fault dislocation. In addition, the dislocate velocity provided by the jack can be manipulated by the buttons on the console platform.

2.2 Sample preparation

Since a water conveyance tunnel would be simulated, tunnel model in circular section was made. Geometric similarity ratio is 1/100 and the density similarity ratio is 1/1 owing to the 1-g model test. Thus, the similarity ratio for the tunnel stress, and strain are 1/100, which can be easily derived by similarity principle.

Based on mentioned similarity relationships above, multiple material tests were conducted to obtain a nice similarity material for modelling. During modelling, constant temperature maintenance for seven days is necessary to ascertain the sufficient strengths. Plaster, water, diatomite, barite powder, and even polypropylene fiber were mixed to simulate tunnel material with a mass ratio following 1: 1.2: 0.6: 0.25: 0.004. The thickness of the model tunnel was 1 cm and the tunnel length is set as 60 cm.

The rock mass was also compounded as tunnel material. Fine sand, sodium silicate, barite powder and water would be used here with a mass ratio of 1: 0.1: 0.6: 0.1, while less sodium silicate was added in component of fault fracture zone for the fracture features with a mass ratio of 1: 0.04: 0.6: 0.1 following the order of rock mass. The component materials for tunnel and rock mass have shown in Fig. 3.

And a prepared tunnel model can be seen in Fig. 4. And the strength parameters of the materials were measured based on shear direct and axis compression tests as listed in Table 1.

The model rock mass was compacted with a plate hammer. The compaction was controlled by a density measured approach. That is, after the compaction of each layer, a cutting ring was used to extract samples of the model rock mass. The sampled cutting ring was then weighted, the weight should be 160 g to satisfy the designated density for the model rock mass.

2.3 Measurement method

As two critical performance indexes, deformation and

Table 1 Strength parameters of the model materials

Units	Weight ($kN \cdot m^{-3}$)	Young's modulus (MPa)	Poison's ratio	Compressive strength (kPa)	cohesion (kPa)	friction (°)
Liner	24.0	300	0.20	143	-	-
Rock mass	25.5	25	0.28	-	5.5	33.02
Fault	19.5	8	0.34	-	4.0	26.56

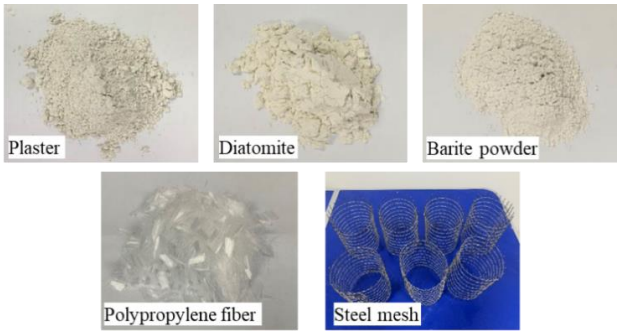

(a) Materials of the tunnel model

(b) Materials of the rock mass and fault model

Fig. 3 Preparation of the model materials

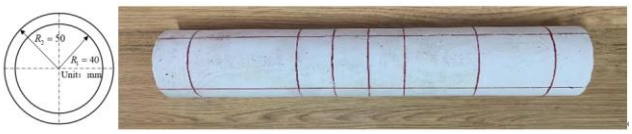

Fig. 4 The prepared tunnel model

failure of tunnel are commonly concerned when a damage potential exists. Thus, displacement and strain for displacement and crack propagation for failure of tunnel were observed in this test to evaluate the stability and reveal the failure mechanism of a fault-crossing tunnel.

2.3.1 Observation of deformations

The target dislocation in the model test was 35 mm for the shear box, which corresponding to a 3.5 m faulting of the prototype project within its 100-year service life. But in practice, the model test continued to a dislocation magnitude of 50 mm. The dislocation velocity was 0.01 mm/s to simulate creep fault movement.

And the deformation of the upper surface of the model was observed with two different techniques. In the first observation technique, the upper surface of the model was covered with gridded white sand, and the deformation feature can be easily identified in the photos that were taken by the CCD camera that was placed directly above.

2.3.2 Measurement of strains

A multi-channel dynamic strain meter was used to collect strains during the test. The layout of the strain gauges was plotted in Fig. 5.

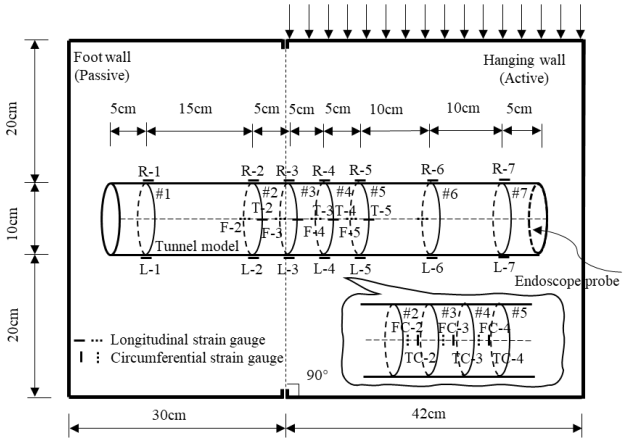

Fig. 5 Layout of the strain gauges

The strain gauges were sticked on the outer surface of this tunnel model following Fig 4. Seven sections for measurement were designed from no. 1 to no. 7. Meanwhile, #2 ~ #5, were considered as the critical sections for measurement owing to the severe damage and deformation of the tunnel near fault. Strain gauges were arranged to the arch, crown, left and right sidewalls labelled as T, F, L, R, TC, FC, in which TC and FC were circumferential strain gauges while the others were longitudinal strain gauges. Necessary calibration to the strain gauges and temperature compensation have been made to ascertain the accuracy of the test.

2.3.3 Crack observation of tunnel

The crack observation of tunnel was performed from both outside and inside the tunnel liner. During the test, the cracks inside the tunnel were recorded with an endoscope, which was patrolling inside the tunnel and operated by the test personnel. As the test completed, the tunnel model would be then dug out from the shear box and thus the cracks outside the liner were observed.

3. Test results

In the test, after every 2 mm dislocation, the deformation, strains, and crack propagation were recorded.

3.1 The rupture propagation of rock mass

Fig. 6 shows the progressive rupture propagation of the

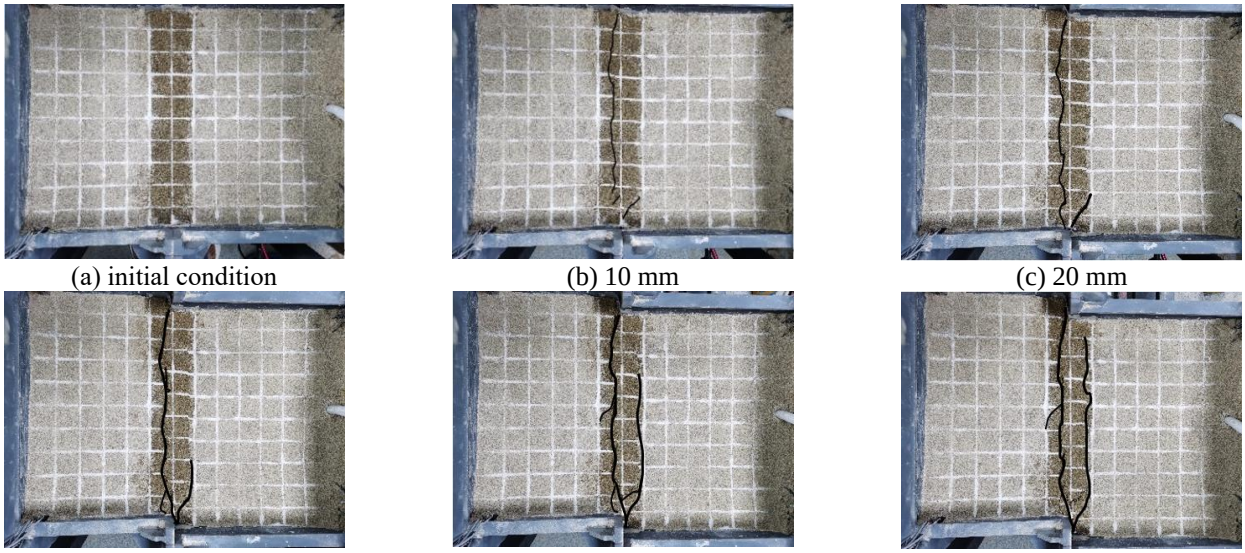

(a) initial condition (b) 10 mm (c) 20 mm

(d) 30 mm (e) 40 mm (f) 50 mm

Fig. 6 Deformed grid and rupture of the model surface during the strike slip faulting (Visible cracks were tracked with black lines)

ground surface with the faulting distances. In the test process, a visible shear crack firstly appeared at a faulting distance of 2 mm. When the dislocation distance reached 10 mm (Fig. 6(b)), a penetrated shear crack band appeared on the foot wall side in the fault zone. Moreover, a second crack appears on fault near hanging wall and gradually propagated along weak contact face between fault and the rock mass of hanging wall (Figs. 6(c)-6(e)). When the fault distance reached 40 mm, it is observed that the initial penetrated shear crack band had gradually deepened and widened. Finally, at a fault distance of 50 mm, the second crack band almost penetrated. It is certain that if the test continued, the second shear band would also be penetrated.

Based on the rock mass displacement observation, it is evident that the most of the shear displacement produced by fault rupture would be limited within the fault fracture zone.

3.2 Strain distribution

Fig. 7 shows the longitudinal strains in the tunnel side walls. For the left side wall, the liners at Section #2 and #3 were in a compression state, while that of Section #1, #4, #5, #6, and #7 were in a tension state.

The maximum compression strain occurred at Section #3 while the maximum tension strain occurred at Section #5. By observing the evolution of the strains with faulting distance, one can notice that the strains at Section #3 and #5 barely increased after the faulting distance reached 25 mm. This indicated that the left side wall of the tunnel began to yield after the faulting distance reached 25 mm, corresponding to a 2.5 m faulting for the prototype tunnel.

For the right sidewall, the liners at Section #4, #5, #6, and #7 were in a compression state, while that of Section #1, #2, and #3 were in a tension state. The maximum compression strain occurred at Section #4 while the maximum tension strain occurred at Section #3. This trend was slightly different from that of the right sidewall. By

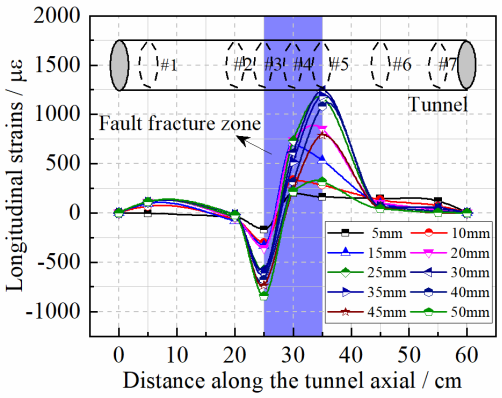

(a) Strains in the left side wall

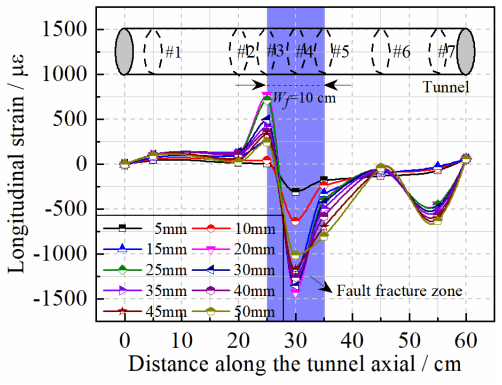

(b) Strains in the right sidewall

Fig. 7 Variation of the longitudinal strains in the tunnel side walls with faulting (tension: + compression: -)

observing the evolution of the strains with faulting distance, one can notice that the strains at Section #3 and #4 barely increased after the faulting distance reached 15 mm. This indicated that the left side wall of the tunnel began to yield after the faulting distance reached 15 mm, corresponding to a 1.5 m faulting for the prototype tunnel.

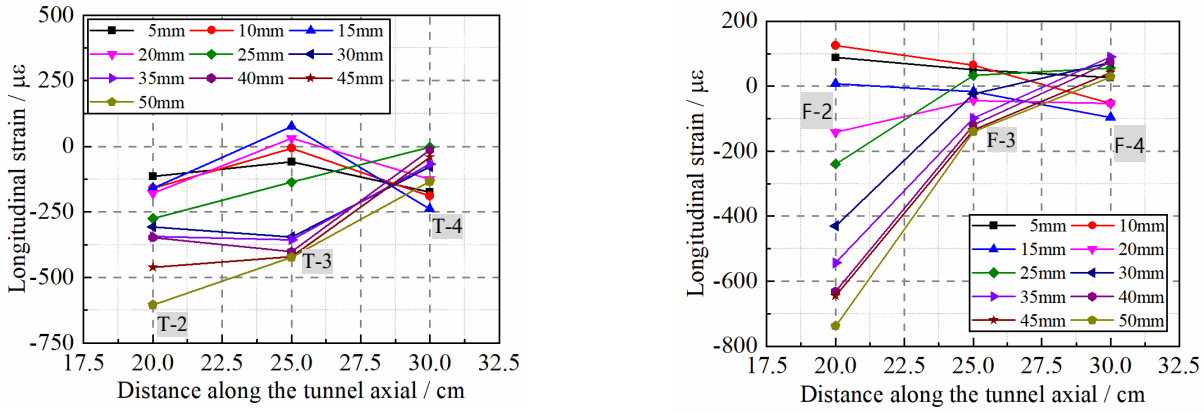

(a) Tunnel roof (b) Tunnel floor

Fig. 8 Variation of the longitudinal strains in the tunnel roof and floor walls with faulting (tension: + compression: -)

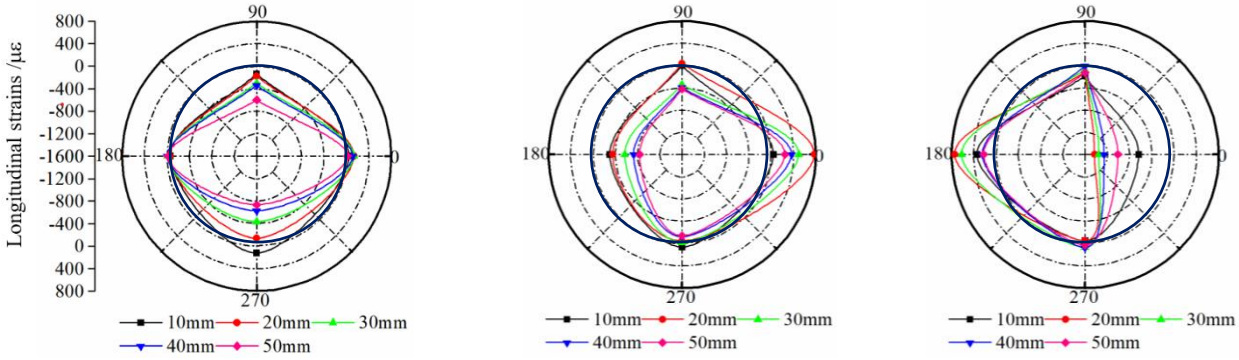

(a) Section #2 (b) Section #3 (c) Section #4

Fig. 9 Longitudinal strains distribution of section #2 to #4(tension: + compression: -)

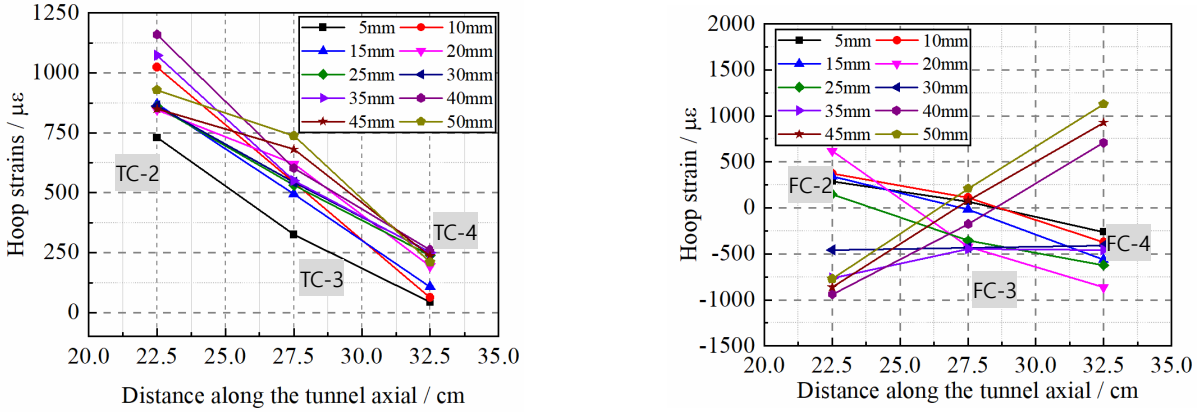

(a) Tunnel roof (b) Tunnel floor

Fig. 10 Variation of the circumferential strains in the tunnel roof and floor walls with faulting (tension: + compression: -)

Fig. 8 shows the strains of the arch and crown of the central sections along longitudinal tunnel. Compared with the strains in the side walls, longitudinal strains in the roof and floor would be significantly smaller.

And Fig. 9 shows the longitudinal strains distribution of Section #2 to #4. A tension state at the right sidewall of Section #3 can be noticed, while the left side wall of which was in a compression state. Correspondingly, the left side wall of Section #4 was in a tension state while its right wall was in a compression state.

And the circumferential strains shown in Fig. 10 demonstrated the arch crown and invert of the tunnel were in a shear state during the strike-slip faulting.

3.3 Crack propagation in tunnel

3.3.1 Cracks inside the tunnel liner

Crack propagation of tunnel was recorded with an endoscope. The crack images have been shown in Fig. 11.

What can be seen is that there is no obvious crack

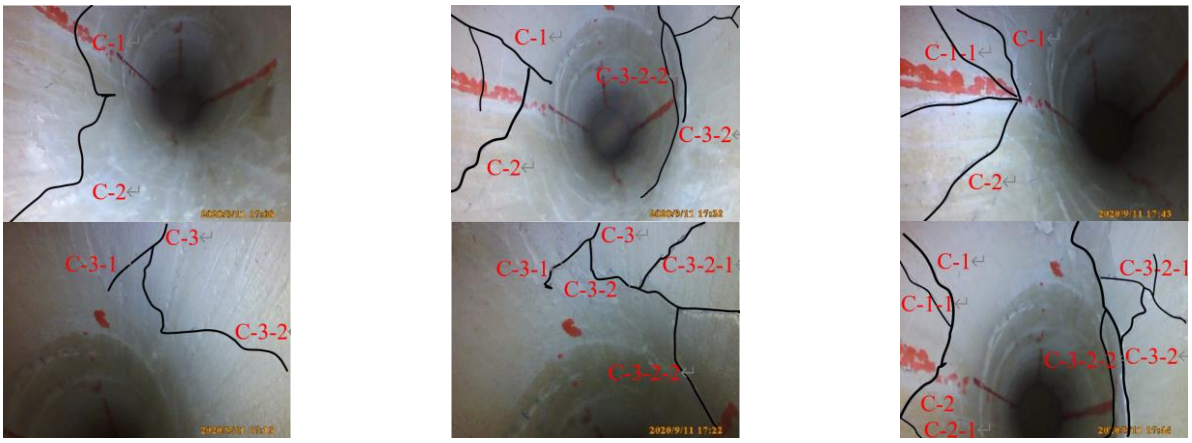

(a) 18 mm (b) 36mm (c) 50 mm

Fig. 11 Progressive crack propagation (see Fig. 12 for the location of the cracks)

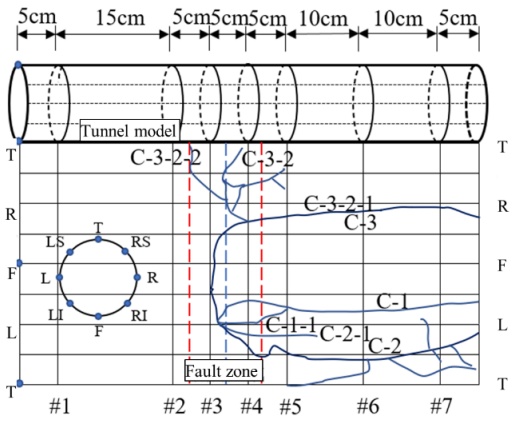

Fig. 12 Panorama view of the developed cracks

Fig. 13 The deformed tunnel model after test

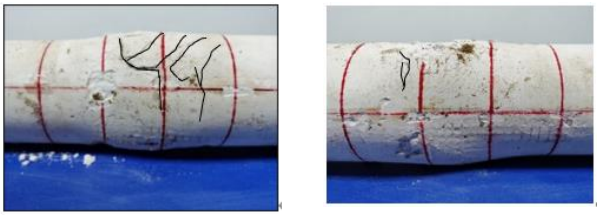

(a) Left side (b) Right side

Fig. 14 The circumferential cracks at the left and right sides of the tunnel (Visible cracks were tracked with black lines)

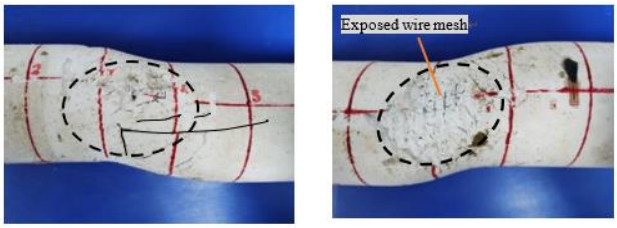

(a) Arch crown (b) inverted arch

Fig. 15 The shear induced spalling at the crown and invert of the tunnel model (Visible cracks were tracked with black lines)

development on inner tunnel before a fault dislocation of 14 mm. When it reached 18 mm, longitudinal cracks appeared near the Sections #3 and #4 (Fig. 11(a)). When the dislocation has reached 36 mm (Fig. 11(b)), the longitudinal cracks were combined with one circumferential crack and gradually extended further to the liner in the hanging wall potion. The circumferential crack within #3 and #4 widened with an increase on fault dislocation (Fig. 11(c)).

The final state of the developed cracks in the liner was plotted in Fig. 12. Circular cracks within the fault fracture zone are more significant. Longitudinal cracks are common along longitudinal tunnel especially in hanging wall, while no clear crack appeared in footwall. Or others, the tunnel damages are concentrated on fault fracture zone, and circular cracks within the fault are main crack pattern.

3.3.3 Cracks tunnel liner

The crack distribution outside of the tunnel liner might be different from that inside the tunnel liner. Clearly, the tested tunnel model (Fig. 13) exhibits a 'S'-shaped deformation form.

The deformation in the liner was mainly focused on the fault shear zone. Multiple longitudinal and circumferential cracks can be recorded respectively. An oval-shaped deformation in tunnel sections appeared owing to the extrusion of the rock mass. In the sidewalls, notable circumferential cracks can be noticed, which confirmed the footage taken by the endoscope from inside of the tunnel. Comparatively, the outside surface of the roof and floor showed distinct shear-induced spalling, which corresponded to the strain results (see Figs. 14 and 15).

Table 2 Unit Parameters of contact faces

c	k_n(GPa)	k_s(GPa)	R_t(GPa)	Bonded slip on/off
contact face-1	16.0	6.0	0.5	on
contact face-2	18.0	12.0	1.3	off

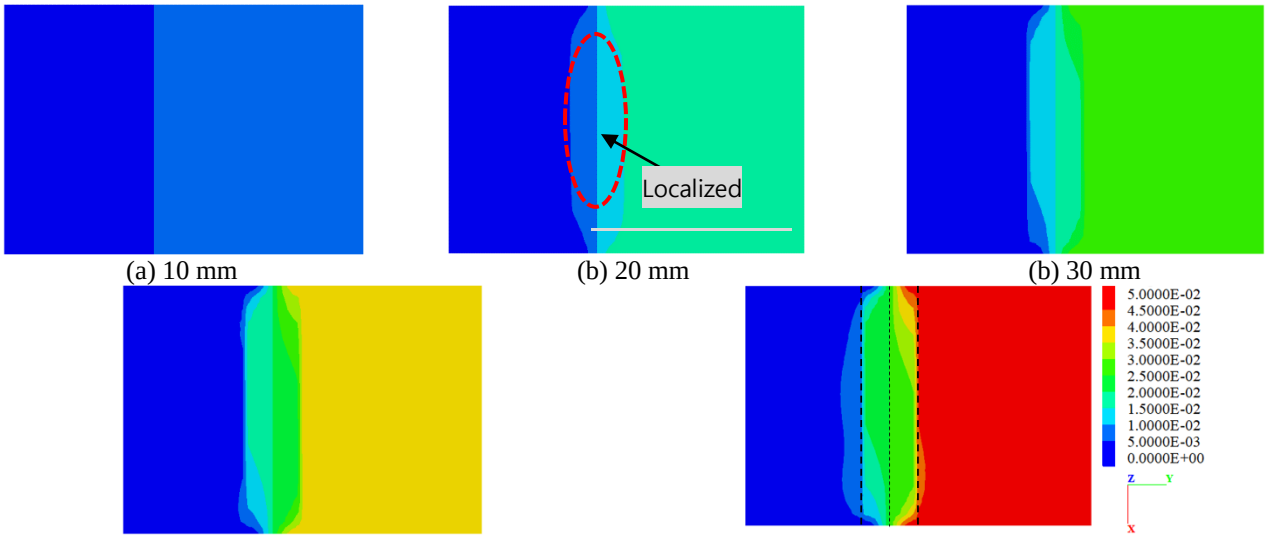

(a) 10 mm (b) 20 mm (b) 30 mm

(d) 40 mm (e) 50 mm

Fig. 17 Calculated displacement contours of overlying surrounding rock mass in numerical analysis

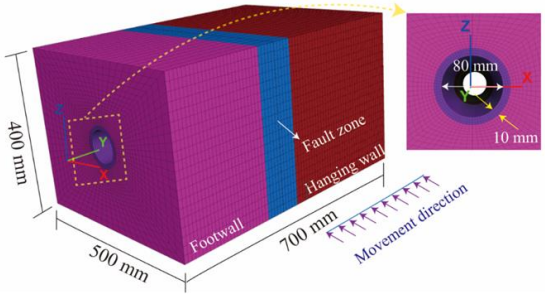

Fig. 16 The FDM numerical model

4. Numerical simulation and verification

4.1 Numerical modeling

A finite difference method (FDM) model was established to numerically reproduce the model test results. The FDM code FLAC3D was used. The dimensions, boundary settings, and mechanical parameters in the FDM model were basically adopted with the help of the physical test.

Fig. 16 shows the numerical model with a fault placed between the fixed block and the moving block whose width equals to 10 cm, with an overall dimension of 40 cm×50 cm×70 cm. The diameter and thickness of the tunnel are 10 cm and 1 cm respectively. The fault dip is set as 90°.

Here in the FDM simulation, the tunnel liner, rock mass, and fault zone were numerically simulated with the solid FDM elements. The M-C constitutive relation was selected to simulate the surrounding rock, while the elastic constitutive model was adopted to assign for tunnel. The mechanical parameters used in the FDM model as mentioned above have been listed in Table 1.

In order to improve the authenticity of the FDM model, there were two special considerations in the numerical simulation. To numerically represent the shear band that emerged in the process of fault dislocation, a group of contact plane (interface) was set at fault zone. Moreover, taking the contact difference at tunnel and rock mass, an interaction was also considered by the application of another group of contact surfaces. Mechanical behaviors of the contact surfaces were decided by the normal and shear parameters. According to direct shear test results based on the test project, the required parameters, such as normal stiffness, k_n and shear stiffness, k_s attributes of the two groups of contact interface were assigned with values listed in Table 2.

4.2 Results

The simulation results were analyzed and verified with test results through 3 aspects, including the ground displacement pattern, the deformation and failure feature, and the stresses and strains of tunnel.

4.2.1 Ground displacement

Fig. 17 shows the displacement contour of the overlying surrounding rock as the fault rupture magnitude reached from 10 mm to 50 mm, respectively.

As can be seen from Fig. 17, when the fault dislocation is less than 10 mm, the displacement on the surface rock mass would be basically continuous. Discontinuous displacement

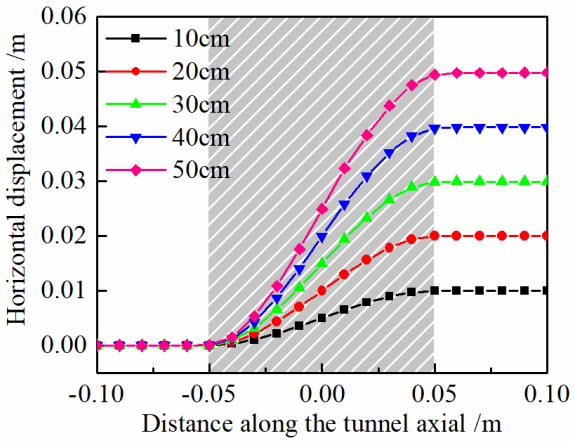

Fig. 18 The calculated horizontal displacement profile at the arch crown of tunnel

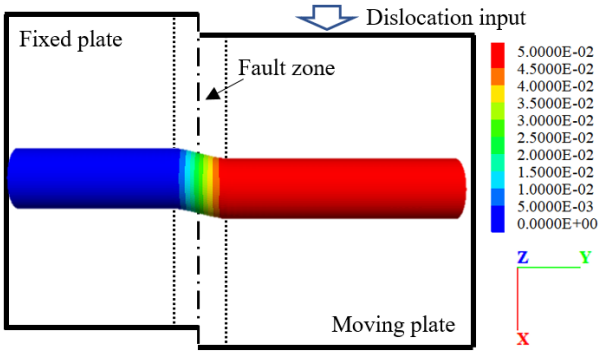

Fig. 19 The calculated horizontal displacement contours at the arch crown of tunnel

gradually emerged in fault core as the rupture faulting reached 10 mm, which corresponded with the penetrated shear crack band observed in the model test. When the rupture faulting distance was approaching 30 mm, the shear displacement was limited within the fault zone. However, as the faulting distance reached a large magnitude of 40 mm, the rock mass at the hanging wall portion and foot wall portion would also be affected. In general, the displacement contours produced by the FEM modelling were in good contrast with the test results shown in Fig. 6.

4.2.2 Displacement profile of tunnel

Fig. 18 shows the calculated horizontal displacement profile of the tunnel roof. The deformation of the tunnel in the fix part (foot wall) was less affected by the fault dislocation, the displacement of this part can be almost ignored. Contrastively, the displacement of the tunnel at hanging wall was almost same as the input boundary displacement. Most of the transition deformation of the tunnel liner presented at fault fracture zone, while there is no obvious at the deformation at the end of two walls.

Fig. 19 shows the final defamation contour of the tunnel liner after 50 mm faulting. A notable S-shaped deformation profile can be logged, which was in good contrast with the test results shown in Fig. 13 at the deformation pattern of the tunnel.

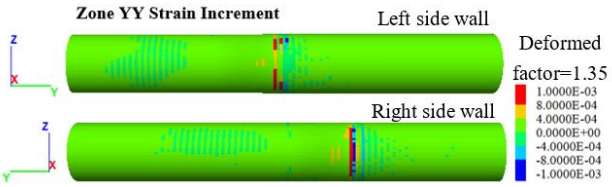

Fig. 20 Calculated longitudinal strain contours along both side walls of the tunnel (tension: + compression: -)

Fig. 21 Calculated maximum shear stress contour on roof and bottom of tunnel (unit in Pa)

4.2.3 Strains and stresses in the tunnel liner

Fig. 20 gives the calculated longitudinal strain contours along both side walls of the tunnel. For the left side wall, notable tensioned strain can be noted in the Section #5. And for the right sidewall, notable tension strain occurred in the Section #3.

Fig. 21 gives the calculated maximum shear stress contour on the roof and bottom of the tunnel. The maximum shear stress at the arch crown and invert of the tunnel at fault core is of significance with a peak value of 40 MPa. The distribution of the maximum shear stress at inverted arch of the tunnel is larger than one at the crown. Notable shear-induced spalling was found in the roof and bottom of the tunnel in the model test (Fig. 15). Therefore, the correctness of the current numerical modelling was verified again. This FDM model thus then can be used in further investigation of the tunnel rupture problem.

5. Conclusions

In this study, a fabricated model test was carried out to research the deformation and failure mechanism when a water conveyance tunnel was suffered from a strike-slip faulting. To verify the test results, a test-based FEM model with consideration of fault fracture zone and weak contact faces was built. Based on the experimental and numerical tests, the deformation pattern and failure mechanism of tunnel, and even fault rupture propagation are revealed furtherly. The conclusions are listed as follows:

(1) For ground deformation, most of the shear deformation occurred within the fault fracture zone. Shear zone cracks can be firstly appeared. Then, the shear crack penetrated in the fault zone with more cracks appeared. The penetrated shear crack band gradually deepen and widen as the fault rupture continued. These crack bands together prompted the formation of the shear deformed zone. The longitudinal profile of the tunnel would exhibit a horizontal ‘S’-shaped deformation form when a tunnel was subjected to strike-slip fault.

(2) With the help of the 'S'-shaped deformation profile, the side walls of the tunnel under fault rupture would mainly experience tension and compression strain state. The convex portions of the S-shaped profile would experience tension strain while the concave portions would in a compression state. Meanwhile, the roof and floor of the tunnel would be in a shear state, where notable shear induced spalling can be noticed in the model test.
(3) The tunnel cracks are more significant in the vicinity of the fault fracture zone. The Longitudinal tunnel cracks at hanging wall and circular cracks at fault fracture zone are more common, while tunnel crack at footwall seems to be seldom significant.
(4) The current study mainly focused on the deformation and stability of an idealized integral tunnel, i.e., without the consideration of any anti-faulting measure. However, the concept of the 'flexible joints' design is becoming more expected as a measure against fault rupture. The structural response of a tunnel with flexible joints under the fault rupture would be the further research target.

Acknowledgments

This work is supported by the National Natural Science Foundation of China (nos. U21A20159, 52079133, 41902288), CRSRI Open Research Program (Program SN: CKWV2019746/KY), MOE Key Lab of Disaster Forecast and Control in Engineering, Jinan University (no. 20200904002), and the Youth Innovation Promotion Association CAS (no. 2019323).

References

Baziar, M.H., Nabizadeh, A., Lee. C.J. and Hung, W.Y. (2014), "Centrifuge modeling of interaction between reverse faulting and tunnel", *Soil Dyn. Earthq. Eng*., **65**, 151-164. https://doi.org/10.1016/j.soildyn.2014.04.008.

Cai, Q.P., Peng, J.M., Ng, C.W., Shi, J.W. and Chen, X.X. (2019), "Centrifuge and numerical modelling of tunnel intersected by normal fault rupture in sand", *Comput. Geotech*., **111**, 137-146. https://doi.org/10.1016/j.compgeo.2019.03.010.

Zhen, C., Qian, S., Gui-min, Z., Mao-chu, Z. and Xian-cheng, M. (2022), "Response and mechanism of a tunnel subjected to combined fault rupture deformation and subsequent seismic excitation", *Transport. Geotech.*, **34**, 100749. https://doi.org/10.1016/j.trgeo.2022.100749.

Huang, J.Q., Zhao, M. and Du, X.L. (2017), "Non-linear seismic responses of tunnels within normal fault ground under obliquely incident P waves", *Tunn. Undergr. Sp. Tech*., **61**, 26-39. https://doi.org/10.1016/j.tust.2016.09.006.

Jalali, H.H., Rofooei, F.R., Attari, N.K.A. and Samadian, M. (2016), "Experimental and finite element study of the reverse faulting effects on buried continuous steel gas pipelines", *Soil Dyn. Earthq. Eng*., **86**, 1-14. https://doi.org/10.1016/j.soildyn.2016.04.006

Kiani, M., Akhlaghi, T. and Ghalandarzadeh, A. (2016), "Experimental modeling of segmental shallow tunnels in alluvial affected by normal faults", *Tunn. Undergr. Sp. Tech*., **51**, 108-119. https://doi.org/10.1016/j.tust.2015.10.005.

Lin, M.L., Chuang, C.F., Jeng, F.S. and Yao, T.C. (2007), The deformation of overburden soil induced by thrust faulting and its impact on underground tunnels", *Eng. Geol*., **92(3-4)**, 110-132. https://doi.org/10.1016/j.enggeo.2007.03.008.

Liu, C., Tang, X., Wei, H., Wang, P. and Zhao, H. (2020), "Model tests of jacked-pile penetration into sand using transparent soil and incremental particle image velocimetry", *KSCE J. Civil Eng*., **24**, 1128-1145. https://doi.org/10.1007/s12205-020-1643-4.

Liu, X.Z., Li, X., Sang, Y.L. and Lin, L. (2015), "Experimental study on normal fault rupture propagation in loose strata and its impact on mountain tunnels", *Tunn. Undergr. Sp. Tech*., **49**, 417-425. https://doi.org/10.1016/j.tust.2015.05.01.

Melissianos, V.E., Korakitis, G.P., Gantes, C.J. and Bouckovalas, G.D. (2016), "Numerical evaluation of the effectiveness of flexible joints in buried pipelines subjected to strike-slip fault rupture", *Soil Dyn. Earthq. Eng*., **90**, 395-410. https://doi.org/10.1016/j.soildyn.2016.09.012.

Melissianos, V.E., Lianos, X.A., Bachas, K.K. Gantes, C.J. (2017), "Experimental investigation of pipes with flexible joints under fault rupture", *J. Constr. Steel Res*., **128**, 633-648. https://doi.org/10.1016/j.jcsr.2016.09.026.

Qiao, Y., Tang, J., Liu, G. and He, M. (2022), "Longitudinal mechanical response of tunnels under active normal faulting", *Undergr. Sp*., **7**(4), 662-679. https://doi.org/10.1016/j.undsp.2021.12.002.

Sabagh, M. and Ghalandarzadeh, A. (2020), "Centrifugal modeling of continuous shallow tunnels at active normal faults intersection", *Transport. Geotech*., **22**, 100325. https://doi.org/10.1016/j.trgeo.2020.100325.

Shahidi, A.R. and Vafaeian, M. (2005), "Analysis of longitudinal profile of the tunnels in the active faulted zone and designing the flexible lining (for Koohrang-III tunnel)", *Tunn. Undergr. Sp. Tech*., **20**, 213-221. https://doi.org/10.1016/j.tust.2004.08.003.

Vazouras, P., Karamanos, S.A. and Dakoulas, P. (2010), "Finite element analysis of buried steel pipelines under strike-slip fault displacements", *Soil Dyn. Earthq. Eng*., **30**, 1361-1376. https://doi.org/10.1016/j.soildyn.2010.06.011.

Vazouras, P., Karamanos, S.A. and Dakoulas, P. (2012), "Mechanical behavior of buried steel pipes crossing active strike-slip faults", *Soil Dyn. Earthq. Eng*., **41**, 164-180. https://doi.org/10.1016/j.soildyn.2012.05.012.

Wang, Q., Geng, P., Li, P., Wang, T. and Sun, W. (2023), "Failure analysis and dislocation-resistant design parameters of mining tunnel under normal faulting", *Eng. Fail. Anal*., **143**, 106902. https://doi.org/10.1016/j.engfailanal.2022.106902.

Wang, T., Geng, P., Li, P., Wang, Q. and Wang, L. (2022), "Deformation and failure of overburden soil subjected to normal fault dislocation and its impact on tunnel", *Eng. Fail. Anal*., **142**, 106747. https://doi.org/10.1016/j.engfailanal.2022.106747.

Yan, Y.S., Chen, Y.H., Wang, C.C., Hwu, Y., Lee, Y.C., Sheu, H. S. andChiang, C.C. (2021), "Faults caused by the fault: Microstructural and mineral characterization of deformation in Chungliao Tunnel, Taiwan, caused by Chishan Fault", *Eng. Geol.*, **292**, 106245. https://doi.org/10.1016/j.enggeo.2021.106245.

Yao, C., He, C., Takemura, J., Feng, K., Guo, D. and Huang, X. (2021), "Active length of a continuous pipe or tunnel subjected to reverse faulting", *Soil Dyn. Earthq. Eng.*, **148**, 106825. https://doi.org/10.1016/j.soildyn.2021.106825.

Zaheri, M., Ranjbarnia, M., Dias, D. and Oreste, P. (2020), "Performance of segmental and shotcrete linings in shallow tunnels crossing a transverse strike-slip faulting", *Transport. Geotech*., **23**, 100333. https://doi.org/10.1016/j.trgeo.2020.100333.

Zeng, G., Geng, P., Guo, X., Li, P., Wang, Q. and Ding, T. (2021), "An anti-fault study of basalt fiber reinforced concrete in tunnels crossing a stick-slip fault", *Soil Dyn. Earthq. Eng*., **148**,

106687. https://doi.org/10.1016/j.soildyn.2021.106687.
Zhong, Z., Wang, Z., Zhao, M. and Du, X. (2020), "Structural damage assessment of mountain tunnels in fault fracture zone subjected to multiple strike-slip fault movement", *Tunn. Undergr. Sp. Tech.*, **104**, 103527. https://doi.org/10.1016/j.tust.2020.103527.

GC